

# Differential geometric methods for examining the dynamics of slow-fast vector fields

Martin Gutschke · Alexander Vais · Franz-Erich Wolter

© Springer-Verlag Berlin Heidelberg 2014

**Abstract** In this work we present computational methods for examining dynamical systems. We focus on those systems being characterized by slow-fast vector fields or corresponding differential algebraic equations that commonly occur in physical applications. In the latter ones scientists usually consider a manifold of admissible physical states and a vector field describing the time evolution of the physical system. The manifold is typically implicitly defined within a higher-dimensional space by a system of equations. Certain physical systems, such as relaxation oscillators, perform sudden jumps in their state evolution when they are forced into an unstable state. The main contribution of the present work is to model the dynamical evolution incorporating the jumping behavior from a perspective of computational geometry which not only provides a qualitative analysis but also produces quantitative results. We use geodesic polar coordinates (GPC) to numerically obtain explicit parametrizations of the implicitly defined manifold and of the relevant jump and hit sets. Moreover, to deal with the possibly high co-dimension of the considered implicitly defined manifold we sketch how GPC in combination with the cut locus concept can be used to numerically obtain an essentially injective global parametrization. This allows us to parametrize and visualize the dynamical evolution of the system including the aforementioned jump phenomena. As main tools we use homotopy approaches in conjunction with concepts from differential geometry. We discuss how to numerically realize and how to

apply them to several examples from mechanics, electrical engineering and biology.

**Keywords** Differential geometry · Dynamical system · Slow-fast vector field · Jump set · Hit set · DAE system · Geodesic polar coordinates · Cut locus

## 1 Introduction

For many physical systems their respective current state at some given time  $t$  can be characterized by an explicit function  $w(t)$ .

The set of all possible states a system may attain has the structure of a space where nearby points correspond to similar states. Additionally, one usually encounters non-linear constraints that reduce the total space of possible states to a subspace of admissible states. Mathematically this situation is modeled within the setting of differential geometry by considering the space of admissible states to be an  $m$ -dimensional regular submanifold  $M$  of a larger ambient space  $\mathbb{R}^k$ . Here  $m$  is the number of degrees of freedom for the physical system, while  $k$  is chosen sufficiently large to capture all relevant parameters of the model under investigation. Moreover, the aforementioned constraints are expressed as equations in the state variables, thereby defining  $M$  implicitly as the zero set of a sufficiently smooth function by

$$M := f^{-1}(0) \quad \text{for } f : \mathbb{R}^k \rightarrow \mathbb{R}^n, \quad m = k - n, \quad k \geq n,$$

where zero is assumed to be a regular value, i.e. that the differential  $df_w$  is surjective at all points  $w \in M$ , implying that  $M$  is embedded in  $\mathbb{R}^k$  as a regular differentiable submanifold of dimension  $m$ , having a tangent space of dimension  $m$  at any of its points. Note that assuming zero to be a regular value does not impose a severe restriction in practice as a well-

M. Gutschke (✉) · A. Vais · F.-E. Wolter  
Welfenlab, Leibniz University Hannover, Hannover, Germany  
e-mail: gutschke@welfenlab.de

A. Vais  
e-mail: vais@welfenlab.de

F.-E. Wolter  
e-mail: few@welfenlab.de

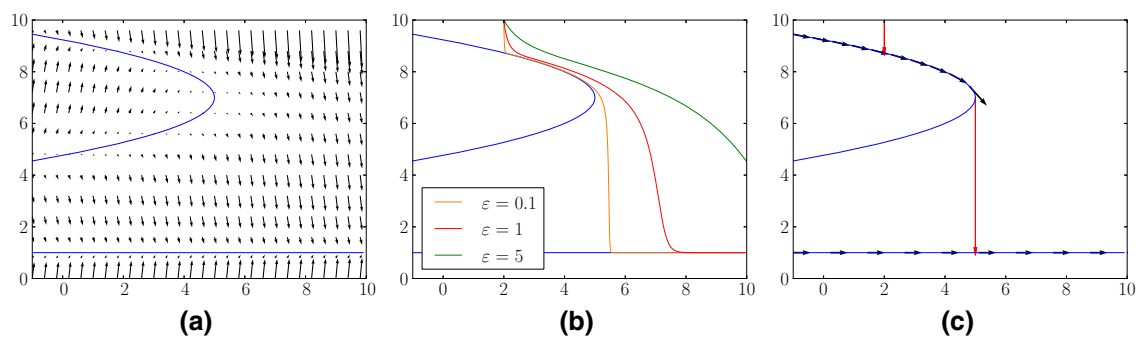


**Fig. 1** Example for a slow-fast vector field

known theorem of Sard assures that singular values form a set of measure zero, see, e.g. [8]. Sard's theorem also implies that adding any arbitrarily small vector to  $f$  will mostly yield a new function where zero will be a regular value.

To model the dynamical behavior of the considered physical system over time, one considers a (smooth) one-parameter family of mappings  $\phi_t : M \rightarrow M$ , describing how a state  $w$  evolves into a state  $\phi_t(w)$  after time  $t$  has elapsed. A more localized description can be given in terms of a tangential vector field  $X_T : M \rightarrow TM$  on  $M$  describing the infinitesimal changes of the system such that

$$\frac{d}{dt}\phi_t(w) = X_T(\phi_t(w)).$$

Such a formulation arises, for example, in the context of Newtonian mechanics where a state in the state space corresponds to generalized position and velocity information while external forces give rise to a vector field that describes the local dynamic behavior of these generalized coordinates. The global description can be recovered by integrating the above ordinary differential equation, thus computing a trajectory  $t \mapsto \phi_t(w)$  of  $X_T$ , providing a time-dependent family of states being initialized with the state  $\phi_0(w)$ .

The aforementioned constraints are in practice often idealizations of a process inducing a fast evolution towards an admissible and stable state. Vice versa, given a description of the fast evolution in terms of a so-called fast vector field  $F$ , one can consider its equilibria, i.e. the points where  $F$  vanishes (c.f. [13]), to define the manifold of admissible states. Complementary  $X$  is denoted as the slow vector field. Thus, the whole dynamical evolution of the non-idealized system can be described in terms of a vector field  $V$  on the larger ambient space  $\mathbb{R}^k$  which is decomposed into a fast and a slow component, i.e.  $V = F + X$ . The fast component  $F$  dominates, leading to a fast flow towards the state manifold  $M$ , where  $F$  vanishes. Thus  $M$  consists of equilibrium points of  $F$ . By looking at the linearization of  $F$  in the points of  $M$ , one can classify those according to whether they constitute stable or unstable equilibria.

As an introductory example let  $V_\varepsilon$  be the following vector field within in  $\mathbb{R}^2$ :

$$V_\varepsilon(x, y) = \begin{pmatrix} 1 \\ \frac{1}{\varepsilon} f(x, y) \end{pmatrix} = \underbrace{\begin{pmatrix} 0 \\ \frac{1}{\varepsilon} f(x, y) \end{pmatrix}}_{F(x, y)} + \underbrace{\begin{pmatrix} 1 \\ 0 \end{pmatrix}}_{X(x, y)}$$

with  $f(x, y) = (x + (7 - y)^2 - 5)(1 - y)$  and a small  $\varepsilon$  as depicted in Fig. 1a. It decomposes into a fast part  $F$  and a slow part  $X$ , where  $F$  vanishes on the submanifold  $M = \{f(x, y) = 0\}$  illustrated by the blue curve. The parameter  $\varepsilon$  controls the speed of the fast component, which increases as  $\varepsilon \rightarrow 0$ .

Consider a fixed initial point  $w \in \mathbb{R}^2$ . Figure 1b shows its trajectory as determined by  $V_\varepsilon$  for various  $\varepsilon$ . Observe that if  $w$  is not contained in a sufficiently small neighborhood of  $M$  then the fast component of  $V_\varepsilon$  will force the corresponding trajectory to quickly approach  $M$ . As  $\varepsilon$  tends to zero, this happens in an almost instantaneous fashion. In the vicinity of  $M$  the trajectory is basically determined by the slow component  $X$  of the vector field which leads towards the vertex of the parabola. At the latter point, which can be seen as a kind of fold with respect to the  $y$  direction, the dynamical evolution will perform a sudden jump vertically downwards along the fast vector field  $F$  until it reaches the lower part of  $M$  where it continues as controlled by  $X$ .

The phenomena occurring in this example for  $\varepsilon \rightarrow 0$ , most notably the jumps occurring at the fold of the manifold, see Fig. 1c, are characteristic of many physical systems that exhibit fast switching behavior, see, e.g. [24].

By combining the implicit description of the admissible state manifold and the description of the dynamical state evolution in terms of a vector field, one obtains a differential algebraic equation (DAE) system

$$f(x, y) = 0 \quad \text{and} \quad g(x, y, X) = 0, \quad (1)$$

where

$$f : \mathbb{R}^m \times \mathbb{R}^n \rightarrow \mathbb{R}^n \quad \text{and} \quad g : \mathbb{R}^m \times \mathbb{R}^n \times \mathbb{R}^k \rightarrow \mathbb{R}^k$$

are given as sufficiently regular functions.<sup>1</sup> Here, the left equation in (1) describes the state or slow manifold  $M \subset \mathbb{R}^k$  while the right one determines a vector field  $X$  on the ambient space. In this description the fast vector field is modeled by jumps within the subspace spanned by the  $y$  variables. The places where jumps occur give rise to the notion of the *jump set* that will be denoted by  $\alpha$  in this paper. More precisely  $p \in \alpha$  if

$$\det \left( \frac{\partial f(p)}{\partial y} \right) = 0, \tag{2}$$

see [5]. We will show how this equation can be used to determine the jump set in practice. The jump itself can be modeled as a map  $\pi : \alpha \rightarrow \beta$  that leaves the variables  $x$  fixed, giving rise to the *hit set*  $\beta = \pi(\alpha)$ .

While fast switching behavior has been studied from a theoretical perspective by many authors, see, e.g. [5–7, 24, 30, 38] comparatively little research has focused on computational approaches, see, e.g. [23].

Computing sub-manifolds being characterized by a singularity condition such as (2) requires an appropriate parametrization. Already in the early days of geometric modeling one would run into situations dealing with singular parametrizations e.g. of spherical triangular spline patches which could be presented by non-singular mappings as well. Here for computations it is important to find a non-singular parametrization, cf. [35]. Analogously, in the present case we can choose a non-singular parametrization of the jump set by describing it as a regular path by tracing its tangent vector.

A main contribution of the present work is to provide a set of geometrically motivated numerical techniques for examining slow–fast vector fields basing on a description in terms of their corresponding differential algebraic equations. Our novel methods provide precise numerical computations of geometric entities being relevant in the given contexts as well as an appropriate visualization. These methods have been designed to be flexible with respect to the dimension and especially independent of the co-dimension of  $M$  to be applicable to a variety of problems. Our approach is applicable to manifolds and vector fields implicitly defined by nonlinear equations by adapting homotopy techniques and numerical continuation methods [1, 37]. Furthermore, we use geodesic polar coordinates [3] to obtain an efficient parametrization and intuitively comprehensible visualization of all computed objects.

A key point in our method is the pre-calculation of the jump and hit sets, thereby enabling an explicit calculation of the jumps induced by the fast vector field. This provides an efficient and numerically stable alternative to traditional

methods which are confined to tracing the slow-fast vector field without making use of the slow manifold. Our geometrically inspired approach has been successfully applied in the context of electrical engineering where it improves the stability of circuit simulators by dispensing with the so-called Tikhonov regularization, see [14, 27, 29]. This paper is an improved version with various additions and extensions of the workshop paper [10]. Besides its applications in electrical engineering, our approach is quite flexible and, therefore, able to investigate a variety of examples inspired by physical applications.

## 2 Basics and notation

Consider a manifold  $M$  embedded in  $\mathbb{R}^k$  and implicitly defined by  $f(w) = 0$  where  $f : \mathbb{R}^k \rightarrow \mathbb{R}^n$ . Here  $k = n + m$  where  $m$  is the dimension of  $M$  while  $n$  is the co-dimension. We will denote by  $f^i : \mathbb{R}^k \rightarrow \mathbb{R}$  the component functions of  $f$ . In compliance with Eq. (1) we will decompose  $w \in \mathbb{R}^k$  according to  $w = (x, y)$  with  $x \in \mathbb{R}^m$  and  $y \in \mathbb{R}^n$  being referred to as the slow and fast variables, respectively.

In this paper we will denote the Jacobian matrix of  $f$  in a point  $p$  by  $J$ , or in components by  $J_{ij} = \frac{\partial f^i(p)}{\partial w^j}$ . The tangent space  $T_pM$  of  $M$  in  $p$  is given by the kernel of  $J$ , i.e.  $T_pM = \{v \in T_p\mathbb{R}^k : Jv = 0\}$ . The orthogonal complement of  $T_pM$  within  $T_p\mathbb{R}^k$  is the normal space which we will denote by  $N_pM$  and is spanned by the columns  $\nabla f^i$  of  $J^T$ . The dimension of  $T_pM$  is obviously  $m$  while the dimension of  $N_pM$  equals the co-dimension  $n$ . As a basis of  $T_p\mathbb{R}^k$  we choose the canonical basis  $e_1, \dots, e_k$ . A basis of  $T_pM$  will be denoted by  $b_1, \dots, b_m$ .

The Jacobian can be used to project any vector  $X \in T_p\mathbb{R}^k$  into  $T_pM$ , see Fig. 2. For the so-called orthogonal projection we write

$$X = X_T + X_N = X_T + \sum_{i=1}^n \nabla f^i u^i = X_T + J^T u \tag{3}$$

with  $u \in \mathbb{R}^n$ . Here  $X_T \in T_pM$  while  $X_N = J^T u \in N_pM$ . Multiplying from the left with  $J$  leads to

$$JX = JX_T + JJ^T u = JJ^T u \implies u = (JJ^T)^{-1} JX.$$

By solving for  $u$  and back-substitution we obtain

$$X_T = X - J^T u = X - J^T (JJ^T)^{-1} JX.$$

The expression  $J^T (JJ^T)^{-1}$  is the Moore–Penrose pseudo-inverse of  $J$  in case  $J$  is of full rank and has more columns than rows. It can be computed efficiently using standard methods such as the singular value decomposition, see [4]. We will denote it in short by  $J^+$ . Thus we can write the orthogonal projection as

$$X_T = X - J^+ JX. \tag{4}$$

<sup>1</sup> Note that contrary to other common uses of the term algebraic, in this context  $f$  and  $g$  are not required to be polynomial functions.

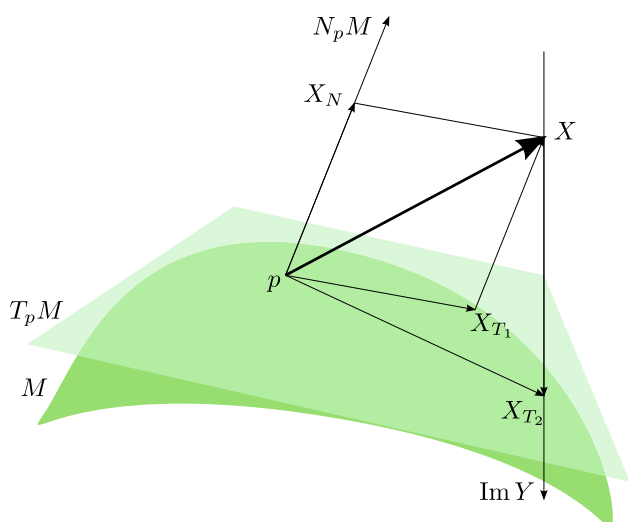


**Fig. 2** Two ways of projecting a vector  $X \in \mathbb{R}^k$  into the tangent space  $T_pM$ . Orthogonal projection yields  $X_{T_1}$  while  $X_{T_2}$  results from a parallel projection along the direction given by  $\text{Im } Y$

Aside from the orthogonal projection we will also need a parallel projection along the subspace spanned by the  $n$  vectors  $e_{m+1}, \dots, e_k$ . We collect those vectors as column vectors forming a matrix  $Y \in \mathbb{R}^{k \times n}$ . Similarly, cf. Eq. (3), we write  $X = X_T + Yu$  for some  $u \in \mathbb{R}^n$ . Multiplying by  $J$  yields

$$JX = JX_T + JYu = JYu \implies u = (JY)^{-1}JX.$$

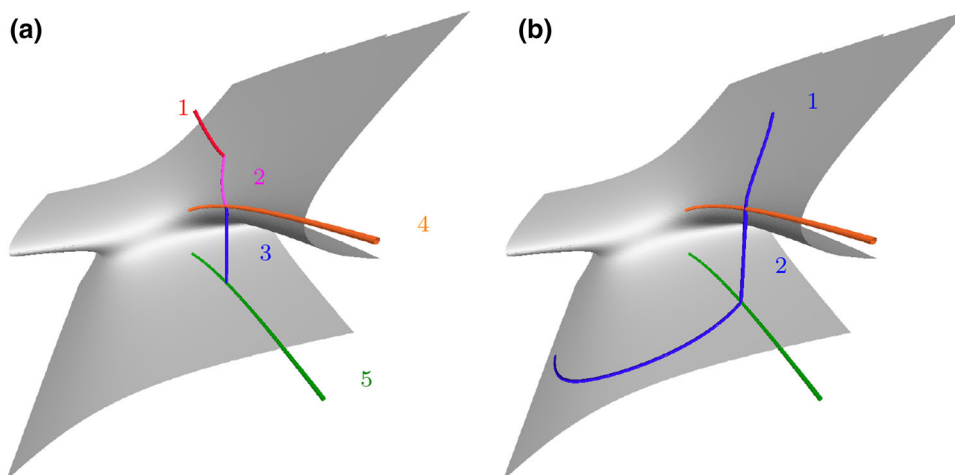
Note that  $JY = \frac{\partial f}{\partial y}$  has full rank for points not lying on the jump set, cf. Eq. (2). Thus we obtain

$$X_T = X - Y(JY)^{-1}JX. \tag{5}$$

### 3 Our approach

Starting with a DAE system as given by Eq. (1), our approach can be split into three phases: preprocessing, tracing and visualization.

**Fig. 3** Overview of the steps of our approach. **a** Preprocessing phase: 1 Determine an initial point on  $M$ . 2 Find the jump set using geodesics. 3 Calculate a corresponding initial point on the hit set. 4, 5 Determine jump and hit set. **b** Tracing phase: starting from a point on  $M$  compute the trajectory of the slow vector field incorporating jumps, see 1 and 2 respectively.



The *preprocessing phase* is used to locate and parametrize the jump and hit sets on the state manifold  $M$ . It consists of the following steps:

- Find an initial point  $w_*$  on  $M$ , see Sect. 3.1.
- Starting from  $w_*$  use geodesics to find a point  $\alpha_0$  on the jump set as discussed in Sect. 3.2.
- Determine the point  $\beta_0$  on the hit set corresponding to  $\alpha_0$  c.f. Sect. 3.3 and trace the jump set  $\alpha$  and the hit set  $\beta$  simultaneously, thereby obtaining suitable parametrizations and the jump map  $\pi : \alpha \rightarrow \beta$ . This is discussed in Sects. 3.4 and 3.5 for one and two-dimensional jump sets, respectively.

In the *tracing phase* we are given an initial point  $\eta_0$  on  $M$ , possibly in terms of geodesic polar coordinates with respect to the aforementioned point  $w_*$ . Using the data collected above allows us to compute the trajectory of the slow dynamic starting in  $\eta_0$  and to approximate the fast dynamic by exploiting the precomputed jump map as discussed in Sect. 3.6. The preprocessing and tracing phases of our approach are graphically summarized in Fig. 3.

Finally, in the *visualization phase*, the parametrization of the resulting trajectory can be visualized and analyzed in various ways to extract useful information. In Sect. 3.7 we will discuss the use of geodesic polar coordinates to visualize our results for two-dimensional manifolds. A discussion of several computational examples is given in Sect. 6.

#### 3.1 Homotopy methods for localizing $M$

In order to perform computations on an implicitly defined manifold  $M$  it has to be localized within the larger ambient space  $\mathbb{R}^k$ . In principle this amounts to finding solutions  $w$  satisfying  $f(w) = 0$ . As the function  $f$  is nonlinear in general, it is challenging to solve this system of equations and furthermore to describe this solution set by a parametrization.

Especially for high co-dimensions it can be difficult to locate even a single point of  $M$ . As a first step, our approach consists of finding a single solution  $w_*$ , i.e.  $f(w_*) = 0$ , by a homotopy method described below. This solution will be used as a starting point for the subsequent computations, especially for introducing a center of geodesic polar coordinates on  $M$ .

In order to find a starting point, we set up a homotopy between the nonlinear system  $f(w) = 0$  and a simpler equation such as  $f(w) - f(w_0) = 0$ . The latter equation can be solved trivially given an arbitrary point  $w_0$  in the ambient space which does not necessarily have to satisfy  $f(w_0) = 0$ . A suitable homotopy can be formulated by linearly interpolating between the two terms using a parameter  $\lambda \in [0, 1]$ :

$$H(w, \lambda, w_0) = f(w) + (\lambda - 1)f(w_0). \tag{6}$$

This is similar to the Newton homotopy which is discussed for example in [1]. An alternative based on the fixed-point homotopy is defined as

$$H(w, \lambda, w_0) = \lambda f(w) + (1 - \lambda)(w - w_0).$$

For a fixed  $w_0$ , the zero set of the function  $H$  is in general a  $(k + 1 - n)$ -dimensional submanifold of  $\mathbb{R}^k \times \mathbb{R}$ . We will call a curve in this submanifold a zero curve of the homotopy function and parametrize it as  $w = w(t)$  and  $\lambda = \lambda(t)$  using a free parameter  $t$ . Substituting these expressions into the homotopy function we obtain the following equation for the zero curve:

$$H(w(t), \lambda(t), w_0) = 0. \tag{7}$$

By construction we have for  $\lambda = 0$ :

$$H(w_0, 0, w_0) = 0,$$

while for  $\lambda = 1$  we obtain

$$H(w_*, 1, w_0) = f(w_*) = 0.$$

Therefore, assuming that  $(w_0, 0)$  and  $(w_*, 1)$  lie on the same connected component of the zero curve, we can reach the point  $(w_*, 1)$  by tracing the path connecting these two points, finally yielding the desired starting point  $w_*$ . Assuming  $H$  to be given by Eq. (6) we differentiate Eq. (7) to yield

$$J(w)\dot{w}(t) + f(w_0)\dot{\lambda}(t) = 0. \tag{8}$$

Note that this equation is a linear system for the vector  $(\dot{w}, \dot{\lambda})$ . It consists of  $n$  equations for  $k + 1$  unknowns. Therefore, assuming  $J$  has full rank, this system has a  $(k + 1 - n)$ -dimensional solution space. Choosing a vector in this subspace defines a suitable tangent vector  $(\dot{w}, \dot{\lambda})$  that can be used to trace the zero curve employing standard ODE solvers or predictor-corrector methods [1, 37]. For many purposes it suffices to assume that the zero curve can be parametrized monotonously by  $\lambda$  and, therefore, we can set  $\dot{\lambda} = 1$ . In this case we choose  $\dot{w}$  to be the uniquely defined vector with

smallest  $L_2$  norm within the solution space of (8), thereby obtaining the initial value problem

$$\dot{w} = -J^+ f(w_0) = -J^+ f(w_0), \quad w_0 = w(0). \tag{9}$$

Assuming that  $J$  has full rank at the points  $w(t)$  it is passing through then  $\dot{w}(t)$  will change continuously. This method can fail due to an unsuitable choice of  $w_0$  if the zero curve containing  $w_0$  does not reach  $\lambda = 1$ . Tracing might also stop in case a singularity occurs. Therefore, the homotopy approach does not guarantee to yield a solution. However, as suggested by the theorem of Sard, these problems can often be easily avoided by applying a small shift to  $w_0$  and restarting the algorithm with the new homotopy function. See also the discussion in [1] for more details on these issues.

Note that the described method can be regarded as an extension of classical homotopy approaches which are designed to handle the computation of isolated zeros of a function  $f : \mathbb{R}^k \rightarrow \mathbb{R}^k$ . In our case, the dimension of the co-domain of  $f$  is  $n$  which is smaller than  $k$ . Therefore, there are many possible zero curves. We pick out a particular curve by choosing its tangent vector according to Eq. (9).

We encountered no difficulties in all of our computational examples using the above strategy. We have tested our method on several geometrically motivated examples and also on some physical examples provided by nonlinear electric circuits [28, 29] which are numerically less well behaved. This suggests that the extended homotopy approach is a useful tool for finding points on implicitly defined manifolds in practice.

### 3.2 Tracing geodesics on an implicit submanifold

Our later computations benefit from a parametrization of the  $m$ -dimensional manifold  $M \subset \mathbb{R}^k$ . Since the co-dimension  $k - m = n$  is possibly high and due to the folded nature of our manifold, this is in general a difficult task. In this setting it is advantageous to introduce geodesic polar coordinates (GPCs) [3]. These are a generalization of the well-known Euclidean polar coordinates which describe the location of a point  $q \in \mathbb{R}^m$  by its distance (denoted by  $s$ ) along a ray through  $p$  emanating from the origin, while the direction of the ray is specified by  $m - 1$  angular parameters  $\varphi_1, \dots, \varphi_{m-1}$ . For the GPCs the origin is replaced by some point  $\gamma_0$  in  $M$  while the rays are replaced by geodesics on  $M$  that emanate from  $\gamma_0$ .

The theorem of Hopf–Rinow [3] implies that on any finite-dimensional, complete and connected Riemannian manifold a given pair of points can be joined by a geodesic. In our context it implies especially that we can cover  $M$  by geodesic polar coordinates. An example illustrating those is shown in Fig. 4, where several geodesics emanating from a central point and some corresponding geodesic circles are depicted.

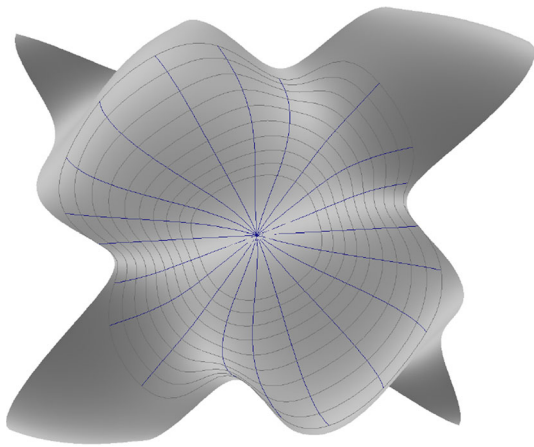


**Fig. 4** Isolines of geodesic polar coordinates

The uniqueness of that kind of parametrization is discussed in Sect. 5.

A geodesic emanating from  $\gamma_0$  is a locally shortest curve  $\gamma : [0, \infty) \rightarrow M$  with  $\gamma(0) = \gamma_0$ , whose initial tangent direction  $\dot{\gamma}(0)$  is given by a unit vector in  $T_{\gamma_0}M$ . It is well known that geodesics are also the locally straightest curves in  $M$ , meaning that their geodesic curvature in  $M$  vanishes, see, e.g. [3]. Moreover, their straightness is characterized by the geodesic differential equations that we will now derive in our setting, where  $M$  is defined implicitly by the equation  $f(w) = 0$ . For an alternative treatment we refer to [15].

First of all, the geodesic  $\gamma : [0, \infty) \rightarrow M \subset \mathbb{R}^k$  is a curve located on the manifold; therefore, it must satisfy the equation  $f^l(\gamma(t)) = 0$  for all  $l = 1, \dots, n$ , cf. Eq. (1). By differentiating this equation with respect to  $t$  we obtain

$$\sum_{i=1}^k \frac{\partial f^l}{\partial w^i} \dot{\gamma}^i = 0,$$

while differentiating again yields

$$\sum_{i,j=1}^k \frac{\partial^2 f^l}{\partial w^i \partial w^j} \dot{\gamma}^i \dot{\gamma}^j + \sum_{i=1}^k \frac{\partial f^l}{\partial w^i} \ddot{\gamma}^i = 0. \tag{10}$$

Since the geodesic  $\gamma$  is a locally straightest curve, which we assume to be parametrized by arc-length, the tangential component of  $\ddot{\gamma}(t)$  vanishes, c.f. [3]. Thus according to Eq. (4) we have  $J^+ J \ddot{\gamma} = \ddot{\gamma}$ . Multiplying the above equation by  $J_{rl}^+$  and summing over  $l$  we obtain

$$\ddot{\gamma}^r = - \sum_{l=1}^n \sum_{i,j=1}^k J_{rl}^+ \frac{\partial^2 f^l}{\partial w^i \partial w^j} \dot{\gamma}^i \dot{\gamma}^j.$$

In order to numerically integrate these equations we need initial values for  $\gamma(0)$  and  $\dot{\gamma}(0)$ . The former are provided by  $\gamma^l(0) = \gamma_0^l$  for  $l = 1, \dots, k$ . In order to determine the latter, we use an orthonormal basis  $(b_i)$  of  $T_{\gamma_0}M$  to construct a unit length vector from the given angular parameters. Note

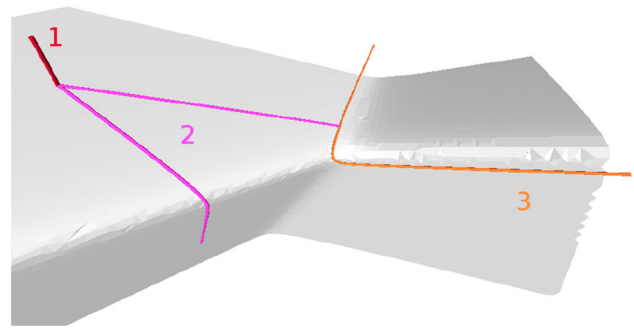


**Fig. 5** Illustration of the method used to find the jump set. 1 Find an initial point on the manifold. 2 Shoot geodesics in order to find the jump set, marked as 3. Only two geodesics are depicted here

that the basis  $(b_i)$  is easily obtained by computing a singular value decomposition of  $J$  or employing Gram–Schmidt orthogonalization.

### 3.3 Initial points on the jump and hit sets

Based on the criterion (2) we use a shooting method to find an initial point of the jump set. More precisely, from a point  $\gamma_0$  on the manifold, which can be chosen as  $\gamma_0 = w_*$  with  $w_*$  as discussed in Sect. 3.1, we shoot geodesics  $\gamma(t)$  until the sign of  $\det\left(\frac{\partial f(\gamma(t))}{\partial y}\right)$  switches. According to the theorem of Hopf–Rinow [3] this procedure must succeed, since geodesics cover the whole manifold. For more details we refer to Sect. 5.

After finishing this procedure we have two types of coordinates of a point  $\alpha_0$  of the jump set, namely its Cartesian coordinates in ambient space as well as its geodesic polar coordinates on the implicitly defined manifold. Figure 5 illustrates the described method.

Using the matrix  $Y$  introduced in Sect. 2, the starting point  $\alpha_0$  of the jump set in combination with the jump space  $\text{Im } Y$  can be used to determine a corresponding jump to a point  $\beta_0$  of the hit set  $\beta$ . More precisely, the set  $\alpha_0 + \text{Im } Y$  defines an  $n$ -dimensional affine subspace containing  $\alpha_0$ . Intersecting this subspace with the manifold  $M$  yields  $\beta_0$ .

In order to formulate this intersection in terms of equations, write  $\alpha_0 = (x_0, y_0)$  where  $x_0 \in \mathbb{R}^m$  and  $y_0 \in \mathbb{R}^n$ . We are interested in determining

$$y_1 \neq y_0 \in \mathbb{R}^n \quad \text{such that } f(x_0, y_1) = 0,$$

explicitly describing the jump in the fast  $y$  variables while the  $x$  variables stay constant. The latter condition is a nonlinear system of  $n$  equations for the  $n$  unknowns in  $y_1$ . Solving this system using a homotopy approach yields the point  $\beta_0 := (x_0, y_1)$  on the hit set. Note that one needs to exclude the trivial solution  $y_1 = y_0$ .

### 3.4 One-dimensional jump and hit sets

Starting from a point  $\alpha_0$  on the jump set our goal is to obtain a parametrization of the jump set  $\alpha$ . In this section we assume  $M$  to be two-dimensional implying the jump set to be one-dimensional. The latter can, therefore, be parametrized by a map  $\alpha : \mathbb{R} \supset I \rightarrow M$  for some interval  $I$ . By abuse of notation we will use  $\alpha$  to denote the jump set as a set or its parametrization depending on the context.

Since  $\alpha \subset M$  and points on  $\alpha$  satisfy the determinant criterion characterizing the jump set, we have the two conditions:

$$f(\alpha(t)) = 0 \quad \text{and} \quad \det \left( \frac{\partial f(\alpha(t))}{\partial y} \right) = 0,$$

which are sufficient to determine  $\alpha$  using a numerical continuation method as follows.

We differentiate the above equations with respect to  $t$ . While the first equation yields  $J\dot{\alpha} = 0$ , computing derivatives of the determinant expression is more involved. The determinant is expressed as

$$\det \left( \frac{\partial f(\alpha(t))}{\partial y} \right) = \sum_{\sigma} \text{sgn}(\sigma) \prod_{r=1}^n \frac{\partial f^r}{\partial y^{\sigma(r)}},$$

where the sum extends over all  $n$ -permutations. Differentiating the last expression with respect to  $t$  yields

$$\sum_{\sigma} \text{sgn}(\sigma) \sum_{s=1}^n \frac{d}{dt} \left( \frac{\partial f^s}{\partial y^{\sigma(s)}} \right) \prod_{\substack{r=1 \\ r \neq s}}^n \frac{\partial f^r}{\partial y^{\sigma(r)}}.$$

Finally, using the chain rule to express  $\frac{d}{dt}(\dots)$  we can write the derivative of the determinant criterion as

$$\sum_{j=1}^k \left( \sum_{\sigma} \text{sgn}(\sigma) \sum_{s=1}^n \frac{\partial^2 f^s}{\partial w^j \partial y^{\sigma(s)}} \prod_{\substack{r=1 \\ r \neq s}}^n \frac{\partial f^r}{\partial y^{\sigma(r)}} \right) \dot{\alpha}^j = 0.$$

Note that the last equation is a linear condition for  $\dot{\alpha}$ . Together with  $J\dot{\alpha} = 0$  this determines a one-dimensional subspace containing  $\dot{\alpha}$ , which is used within classical ODE solvers or predictor-corrector methods. The only degrees of freedom left are the length of  $\dot{\alpha}$  and its sign. In order to parametrize the jump set by arc length one can enforce the condition  $\|\dot{\alpha}\| = 1$ . The sign ambiguity allows us to choose the tracing direction.

Like the jump set, the hit set can be parametrized as  $\beta : \mathbb{R} \rightarrow M$ . From Sect. 3.3 we already know an initial point  $\beta_0$  with  $\beta(0) = \beta_0$ . It is advantageous to compute  $\alpha$  and  $\beta$  simultaneously within a numerical continuation method, with the necessary tangent direction  $\dot{\beta}$  being obtained as follows. Denoting the jump map by  $\pi(x, y) = (x, \pi^y(x, y))$ , we fix the parametrization of  $\beta$  by

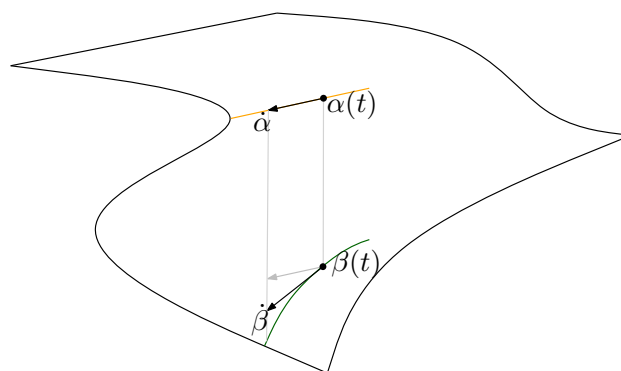


Fig. 6 Computing tangent information for the hit set

$$\beta(t) = \pi(\alpha(t)). \tag{11}$$

Since  $\beta(t)$  lies on the manifold, we have

$$f(\alpha^x(t), \pi^y(\alpha(t))) = 0,$$

where we have denoted by  $\alpha^x$  the slow component of  $\alpha$ . By differentiating with respect to  $t$  we obtain

$$\frac{\partial f}{\partial x} \dot{\alpha}^x + \frac{\partial f}{\partial y} d\pi^y \dot{\alpha} = 0 \Rightarrow d\pi^y \dot{\alpha} = - \left( \frac{\partial f}{\partial y} \right)^{-1} \frac{\partial f}{\partial x} \dot{\alpha}^x.$$

Thus, considering (11), the derivative  $\dot{\beta}$  is given as

$$\dot{\beta} = d\pi \dot{\alpha} = \begin{pmatrix} \text{id}_{\mathbb{R}^m} & 0 \\ d\pi^y \end{pmatrix} \begin{pmatrix} \dot{\alpha}^x \\ \dot{\alpha}^y \end{pmatrix} = \begin{pmatrix} \dot{\alpha}^x \\ - \left( \frac{\partial f}{\partial y} \right)^{-1} \frac{\partial f}{\partial x} \dot{\alpha}^x \end{pmatrix}.$$

As indicated in Fig. 6, the last equation can be geometrically interpreted as applying the projection in Eq. (5) to the vector  $\dot{\alpha}(t)$ , where the latter is considered as lying in  $T_{\beta(t)}\mathbb{R}^k$ , i.e.

$$\dot{\beta}(t) = \dot{\alpha}(t) - Y(JY)^{-1} J\dot{\alpha}(t), \tag{12}$$

with the Jacobian  $J$  of  $f$  being evaluated at  $\beta(t)$ .

Note that the parametrized one-dimensional jump and hit sets can be represented compactly by B-splines for further processing, see e.g. [34].

### 3.5 Multi-dimensional jump and hit sets

In case the state manifold  $M$  has dimension  $m \geq 3$  the jump set is no longer a curve and thereby needs to be parametrized in terms of a multivariable map  $\alpha : \mathbb{R}^{m-1} \supset U \rightarrow M$ . The considerations of the previous section still apply to constructing an individual one-dimensional curve lying within the jump set. However, the corresponding equations are not sufficient to determine the tangent direction of the curve uniquely.

In order to overcome this difficulty, we can use geodesic polar coordinates to obtain a parametrization of the jump set.

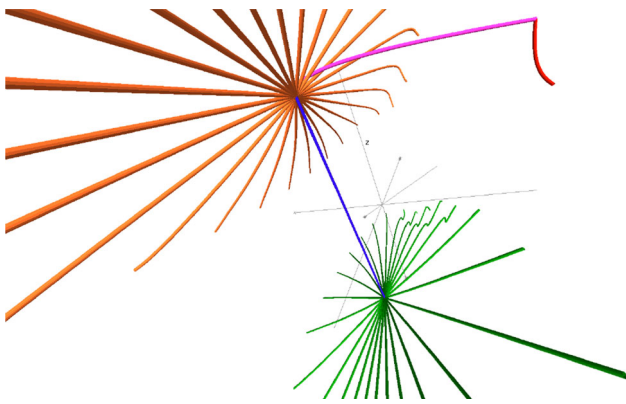


**Fig. 7** A two-dimensional jump set, shown in orange, captured by computing geodesics radially emanating from an initial point  $\alpha_0$ . The corresponding curves on the hit set emanating from  $\beta_0$  are shown in green

More precisely, let us introduce the function  $\widehat{f} : \mathbb{R}^k \rightarrow \mathbb{R}^{n+1}$  given by

$$\widehat{f}(w) = \left( f(w), \det \left( \frac{\partial f(w)}{\partial y} \right) \right).$$

The equation  $\widehat{f}(w) = 0$  defines the jump set implicitly as an  $(m - 1)$ -dimensional submanifold of  $M \subset \mathbb{R}^k$ . Within this submanifold we can compute geodesics as described in Sect. 3.2 by using  $\widehat{f}$  instead of  $f$ .

Figure 7 illustrates the method for a two-dimensional jump set. Several geodesics that emanate from an initial point  $\alpha_0$  have been computed, thus inducing geodesic polar coordinates. As discussed in Sect. 3.4, the hit set is parametrized simultaneously by tracing the corresponding projections of those geodesics using Eq. (12). Note that this approach includes the one discussed in the previous section as a special case.

### 3.6 Tracing a vector field on the slow manifold

Assume a vector field  $X : M \rightarrow \mathbb{R}^k$  to be defined implicitly by

$$g(w, X) = 0 \quad \text{where} \quad g : \mathbb{R}^k \times \mathbb{R}^k \rightarrow \mathbb{R}^k$$

is assumed to be differentiable and to have an invertible partial differential with respect to  $X$  along  $M$ . At any point  $w \in M$  we can project  $X$  onto  $T_w M$  to yield a vector field  $X_T : M \rightarrow TM$  on  $M$ , which is accomplished using Eq. (5).

We will assume that  $X_T$  is a description of the slow vector field on  $M$ . Starting from a given point  $\eta_0$  on the slow manifold  $M$ , our goal is to construct the trajectory  $\eta : \mathbb{R} \rightarrow M$  of  $X_T$  with  $\eta(0) = \eta_0$ . Denote by  $X(t) \in \mathbb{R}^k$  the values of the vector field  $X$  described above along  $\eta$ . Thus we have

$$f(\eta(t)) = 0, \quad g(\eta(t), X(t)) = 0.$$

The functions  $\eta$  and  $X$  can be computed in parallel by numerically integrating the following system of ordinary differential equations

$$\begin{aligned} \dot{\eta} &= X - Y(JY)^{-1} JX \\ \dot{X} &= - \left( \frac{\partial g}{\partial X} \right)^{-1} \frac{\partial g}{\partial w} \dot{\eta}. \end{aligned}$$

Note that the equation for  $\dot{\eta}$  describes  $\eta$  as a trajectory of the slow vector field  $X_T$  while the equation for  $\dot{X}$  follows from differentiating  $g(\eta(t), X(t)) = 0$  with respect to  $t$  and solving for  $\dot{X}$ .

Initial conditions are provided by the given point  $\eta(0) = \eta_0$  and  $X(0) = X_0$ . In order to determine  $X_0$  one has to solve the nonlinear system  $g(\eta_0, X_0) = 0$  for  $X_0$ . The latter step can be done using a homotopy approach analogous to Sect. 3.1.

### 3.7 Visualizing objects on $M$ using GPCs

Since subsets of  $M$  such as the jump set, the hit or the slow parts of the computed trajectories may lie within a potentially high-dimensional ambient space  $\mathbb{R}^k$ , it is in general difficult to visualize and understand their shapes and their relative position to each other in terms of a low-dimensional projection. For simplicity in the following we assume such subsets to be described in terms of a collection of curves. As those curves lie within the  $m$ -dimensional manifold  $M \subset \mathbb{R}^k$  where  $m < k$  it is advantageous to visualize them via an  $m$ -dimensional parametrization of  $M$ . Since  $M$  is defined implicitly such a parametrization is not readily available. In particular despite the locally valid conclusion of the theorem on implicit functions, due to the generally folded nature of  $M$ , one cannot expect to be able to globally construct such a parametrization in terms of a naive approach aiming at closed form expressions by solving the defining equation  $f(w) = 0$  for  $k - m$  coordinates.

However, geodesic polar coordinates naturally suggest themselves to be used within this context. Reducing the dimensionality from  $k$  to  $m$  by visualizing objects on  $M$  using polar coordinates allows for a better comprehension of their geometrical and topological relationships. If the manifold is two-dimensional one can intuitively picture this approach as a means to flatten the manifold and the objects on it onto a plane. This flattening is essentially even possible in case  $M$  is not simply connected, cf. Sect. 5.

Given a curve  $\alpha$  on  $M$ , computing its polar coordinates with respect to a point  $p \in M$  amounts to the following problem: let  $\gamma : \mathbb{R} \times S^{m-1} \rightarrow M$  be the map that sends the polar coordinates  $(s, \varphi)$  to the point  $\gamma(s, \varphi)$  in  $M$ . The latter is computed by calculating a geodesic curve of length  $s$  emanating from  $p$  in direction  $\varphi$  and taking its endpoint as discussed



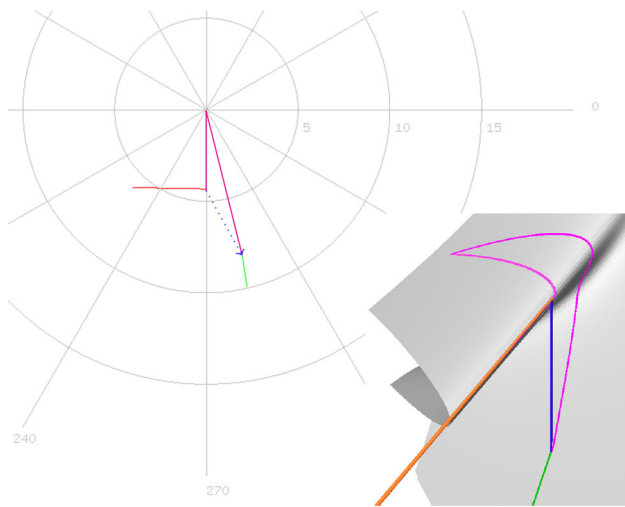


**Fig. 8** Visualization via geodesic polar coordinates. The jump set and corresponding hit set are shown in *orange* resp. *green*. Additionally two geodesics are drawn in *pink*. The *blue dotted arrow* indicates the correspondence between two points related by a jump

in Sect. 3.2. We are now interested in finding the preimages of all points  $\alpha(t)$  under  $\gamma$ , thereby solving the equation

$$\gamma(s(t), \varphi(t)) = \alpha(t)$$

for the unknown functions  $(s, \varphi) : \mathbb{R} \rightarrow \mathbb{R} \times S^{m-1}$ . Differentiating the last equation with respect to  $t$  one obtains

$$\frac{\partial \gamma}{\partial s} \dot{s} + \frac{\partial \gamma}{\partial \varphi} \dot{\varphi} = \dot{\alpha}.$$

This system of linear equations can be solved for  $(\dot{s}, \dot{\varphi})$  since  $\dot{\alpha}$  is tangential to  $M$  provided that  $\frac{\partial \gamma}{\partial \varphi}$  has full rank. Thus one can compute  $s(t), \varphi(t)$  using classical numerical continuation methods, assuming that the coordinates of an initial point are known. Note that this is the case for the jump set which is found using geodesics as described in Sect. 3.3. Otherwise one can adapt the homotopy approach described in [25].

Note that problems can arise if  $\frac{\partial \gamma}{\partial \varphi}$  becomes rank deficient during the numerical continuation, indicating the presence of points which are said to be conjugate to  $p$  [3]. In this case, it is beneficial to allow for a more flexible parametrization of  $\alpha$  by introducing a free parameter  $\lambda$ , i.e. setting  $t = t(\lambda)$  as discussed in [25].

Figure 8 shows an example, visualizing the jump and hit set on a two-dimensional manifold using geodesic polar coordinates.

#### 4 Finding GPC of points on the hit set

In order to represent a submanifold  $S \subset M$  in terms of geodesic polar coordinates centered at a point  $p \in M$ , it is in

general a difficult boundary value problem to find suitable initial values for a geodesic starting in  $p$  such that it leads to some given point  $q \in S$ . More specifically, using the notation introduced in the last section one needs a distance parameter  $r$  and a set of angular parameters  $\psi$  such that

$$\gamma(r, \psi) = q \quad (13)$$

Looking at the special submanifolds such as the jump and hit sets whose calculation was described in the previous sections, the mentioned difficulty does not apply to the jump set, since it can easily be found by tracing geodesics while checking for the determinant criterion (2) to be fulfilled. However, for the hit set such an implicit criterion is not directly available, since it is merely characterized by its relation to the jump set in terms of a projection that leads out of the manifold  $M$  through the ambient space. Therefore, obtaining a geodesic on  $M$  connecting the GPC center  $p$  with some point on the hit set is a challenging task.

Note that in case the implicitly defined manifold  $M$  consists of multiple connected components, two submanifolds are contained within the same connected component if and only if they can be connected by a curve in  $M$ . In this context our numerical approaches exploiting the geodesic flow has the potential to yield insights into the structure of the connected components of  $M$ . In the following we assume for simplicity the relevant part of the hit set to lie in the same component as  $p$ .

One can start by noting that any point  $q$  of the hit set is characterized by two properties: (1) it lies on the manifold  $M$  and (2) its  $x$  components coincide with the  $x$  components of some point  $\tilde{q}$  lying on the jump set. The first property is already fulfilled by the assumption that  $q$  can be described in terms of GPC  $r, \psi$  as in Eq. (13). Using this, the second property can be written as

$$\rho(\gamma(r, \psi)) - \rho(\tilde{q}) = 0,$$

where  $\rho$  denotes the projection  $\mathbb{R}^m \times \mathbb{R}^n \rightarrow \mathbb{R}^m, (x, y) \mapsto x$ . An approach to solving this non-linear equation for the unknowns  $(r, \psi)$  can be obtained by a suitable homotopy method. However, for our purposes it has proved convenient to introduce more flexibility by assuming that the point  $\tilde{q}$  is allowed to vary on the jump set while also being described in terms of GPC, i.e.  $\tilde{q} = \gamma(s, \varphi)$  for some parameters  $s, \varphi$ . Exploiting the determinant criterion (2) we can formulate our problem as the search of the zero set of the function

$$F(r, \psi, s, \varphi) = \begin{pmatrix} \det \frac{\partial f}{\partial y}(\gamma(s, \varphi)) \\ \rho(\gamma(r, \psi)) - \rho(\gamma(s, \varphi)) \end{pmatrix}$$

Note that this  $F$  is a function of  $2m$  unknowns with a  $(m+1)$ -dimensional range; therefore, under a general non-degeneracy assumption the theorem on implicit functions assures that its zero set is  $(m-1)$ -dimensional corresponding

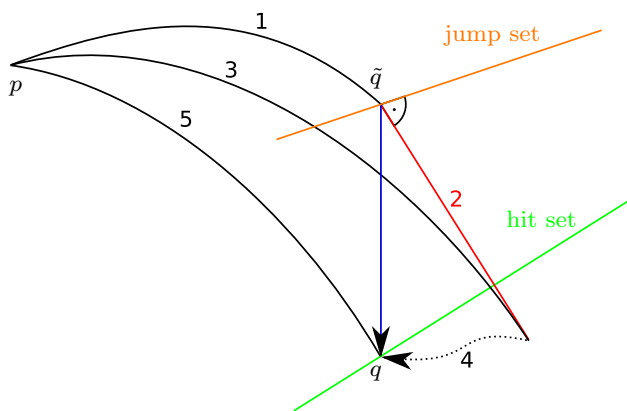


**Fig. 9** Schematic diagram for determining the GPC of a point on the hit set using a homotopy

to the fact that the hit set is a hypersurface in  $M$ . Embedding this function into a Newton homotopy with

$$H(r, \psi, s, \varphi, \lambda) = F(r, \psi, s, \varphi) + (\lambda - 1)F(r_0, \psi_0, s_0, \varphi_0)$$

for some set of initial values  $\omega_0 = (r_0, \psi_0, s_0, \varphi_0)$ , we can search for a solution by taking the derivative of the equation  $H(\omega(t)) = 0$  with respect to  $\lambda$  thereby obtaining

$$dF(\omega(t)) \cdot \dot{\omega}(t) + F(\omega_0) = 0$$

This can be used to yield

$$\dot{\omega}(t) = -dF(\omega(t))^{+} F(\omega_0) \tag{14}$$

using the pseudo-inverse of the differential of  $F$ . The latter can be expressed in matrix block form as

$$dF = \begin{pmatrix} 0_{1 \times k} & \frac{\partial}{\partial \omega} \left( \det \frac{\partial f}{\partial y} \right) \\ d\rho & -d\rho \end{pmatrix} \begin{pmatrix} d\gamma(r, \psi) & 0_{k \times m} \\ 0_{k \times m} & d\gamma(s, \varphi) \end{pmatrix}$$

where the differential of the projection  $d\rho$  is given by the matrix  $(I_{m \times m} | 0_{m \times n})$  with  $I$  and  $0$  in the above expressions denoting the identity and zero matrices with dimensions as given by the respective subscripts. Note that for the derivative of the determinant expression one can draw upon the results of Sect. 3.4.

To successfully realize the above procedure basing on Eq. (14) one needs initial values for the vector  $\omega(0) = \omega_0$ , consisting of suitable guesses of the GPCs  $(s_0, \varphi_0)$  and  $(r_0, \psi_0)$ . Following the situation indicated in Fig. 9 we consider the point  $\tilde{q}$  on the jump set to be reached by a geodesic (1) starting in  $p$  whose length and starting direction determine  $r_0$  and  $\psi_0$ . Initial guesses for the parameters  $s_0, \varphi_0$  can be obtained from an algorithm based on the heuristic observation that one is likely to approach the hit set as one moves on a geodesic contained in  $M$  orthogonally away from the jump set, starting in  $\tilde{q} = \gamma(r_0, \psi_0)$ .

Since a sufficient distance is not known a-priori, one can start with a rough estimate based on the Euclidean distance

between the jump and hit sets in ambient space. In case no convergence is obtained, one can employ an iterative search strategy by doubling the search distance in each iteration. Since the jump set is a hypersurface in  $M$  and there are two possible directions in the tangent space of  $M$  orthogonal to this hypersurface, moving on geodesics away from the hypersurface is quite natural in the given context. More specifically we consider the geodesics  $\tilde{\gamma}_{\pm}$ , illustrated by the curve (2) in Fig. 9, starting in  $\tilde{q}$  with direction  $\pm \nu$  where  $\nu$  is the normal of the jump set in  $M$ . The direction of the vector  $\nu$  is determined by the property of being orthogonal to the kernel of  $d \left( \det \frac{\partial f}{\partial y} \right)$  within the kernel of  $df$ .

After tracing these geodesics for some distance  $s_g$  corresponding to the current estimate we obtain a point  $q_0 = \tilde{\gamma}(s_g)$  whose GPC with respect to the original GPC system centered at  $p$  serve as suitable initial values for  $s_0$  and  $\varphi_0$ . Note that the latter are not immediately available, since there is no closed form expression relating parameters of geodesics starting in  $p$  with those starting in  $\tilde{q}$ . However,  $s_0, \varphi_0$  can be easily obtained by pulling the end point of the known geodesic from  $p$  to  $\tilde{q}$  along  $\tilde{\gamma}$  until reaching  $\tilde{\gamma}(s_d)$  using the method described in Sect. 3.7, thereby yielding the geodesic (3).

Now, having obtained the initial values  $(r_0, \psi_0)$  and  $(s_0, \varphi_0)$ , the homotopy (4) yields the desired parameters  $r, \psi$  of the geodesic (5) connecting  $p$  with the point  $q$  on the hit set.

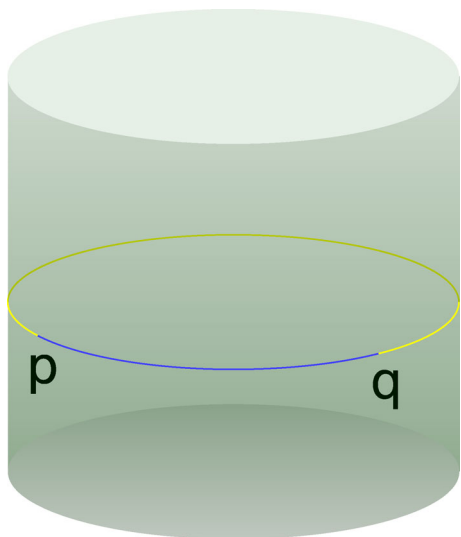
### 5 Cut locus as a boundary of geodesic parametrization

In Sect. 3.7 we have applied GPC as way to parametrize the implicitly defined manifold  $M$ . We used this parametrization to localize and understand the topological relation and partly the distance relation between different geometric objects on  $M$ . It turns out that GPCs in combination with the cut locus concept outlined in the following provides a natural and powerful tool to parametrize and visualize geometric objects within  $M$  by providing an essentially global injective parametrization of each connected component of  $M$ .

The theorem of Hopf–Rinow implies that GPC with respect to some fixed point  $p \in M$  cover the whole manifold  $M$  in the sense that the corresponding map  $\gamma : \mathbb{R} \times S^{m-1} \rightarrow M$  is surjective, provided that  $M$  is connected and complete as a metric space. In our case dealing with unbordered topologically closed differentiable submanifolds of  $\mathbb{R}^k$  defined implicitly, the latter condition is fulfilled where we refer to [32] for an in-depth discussion of the underlying topological arguments involved. Furthermore, in this case Hopf–Rinow guarantees the existence of a connecting geodesic between any two points  $p, q \in M$ , thereby allowing us to define the Riemannian distance between  $p$  and  $q$  as the minimal length of such geodesics.

As discussed in the last section, this allows us to represent all relevant submanifolds of  $M$  within a visualization such as the one exemplified in Fig. 8. However, while sufficiently short geodesics emanating from  $p$  do not intersect, in our case they can be extended arbitrarily, such that intersections become possible and yield redundancies in the visualization. In fact several global and local phenomena can occur that are not observed in the familiar Euclidean setting, where geodesics are straight lines.

Consider first the sphere  $M = S^2$  where geodesics starting at some point  $p$  meet in the diametrically opposite point  $q$  after a distance of  $\pi$ . Extending those even further one sees that due to the resulting periodicity  $q$  has any element in the set  $(2\mathbb{Z} + 1)\pi \times S^1$  as valid GPC, yielding a highly redundant description.



As a similar elementary example the figure above shows a cylinder with two different geodesics connecting  $p$  with another point  $q$ , yielding two GPCs for  $q$ . In fact, this example also exhibits periodic behavior that generates an infinity of alternative GPCs for  $q$ .

Observe that, while the cylinder is flat in terms of Gaussian curvature, geodesics meet due to its global topological structure. However, geodesic connections can also become non-unique in the local presence of Gaussian curvature as shown in Fig. 13a: The black curve represents a submanifold of  $M$  that is to be visualized in terms of GPC with respect to  $p$ . The red curve is the focal curve  $f_p$  of  $p$ , also known as the conjugate locus of  $p$ . It consists of all points  $u = \gamma(s_u, \varphi_u)$  where the rank of  $d\gamma_{(s_u, \varphi_u)}$  is not maximal, cf. [3]. Geodesics are definitely not distance-minimal beyond the conjugate locus, see [32] for a proof lacking variational arguments. Note that while there is just a single geodesic connecting  $q_1$  and  $p$ , the points  $q_2$  and  $q_3$  have two, resp. three different geodesic connections to  $p$ . Therefore we obtain the situation depicted in Fig. 13b showing that the segment  $q_2, q'_2$  is represented by three different segments in terms of our GPC visualiza-

tion. Finally, note that extending the allowed length of the considered geodesics even further, the situation can become much more intricate due to the presence of multiple focal curves.

All of the above examples suggest to restrict the length of geodesics in order to avoid redundancies in the visualization while still ensuring full coverage of the manifold  $M$  with GPC. A natural means to achieve this goal makes use of a concept introduced by Poincaré [19] known as the cut locus.

In general, the cut locus  $C_A$  of some closed set  $A \subset M$  can be defined as the closure of the set of all non-extenders with respect to  $A$ , the latter being defined as points  $q \in M \setminus A$  such that the shortest connection from  $A$  to  $q$  fails to extend to a shortest path beyond  $q$ . An alternative description of  $C_A$  is given in terms of the closure of the set of Picas with respect to  $A$ , c.f. [31,32]. Here a point  $q \in M \setminus A$  is called a Pica if there exist at least two shortest paths to  $A$ . In our case it suffices to consider the cut locus with respect to  $A = \{p\}$  with  $p$  being the GPC center. We will denote it by  $C_p$ . An example for the cut locus is shown in Fig. 10 on the right.

Based on this definition it is apparent that for a fixed  $\varphi \in S^1$  each geodesic  $s \mapsto \gamma(s, \varphi)$  of length  $L$  radially emanating from  $p$  is the shortest connection from  $p$  to its endpoint  $\gamma(L, \varphi)$  as long as  $\gamma([0, L], \varphi)$  does not intersect  $C_p$ . One also says such a geodesic is distance minimizing with respect to  $p$ . Denoting the maximal length fulfilling this property by  $s_c(\varphi)$ , one generally observes the shortest connection to change abruptly if the geodesic is extended beyond  $s_c(\varphi)$ .

Limiting the length of all geodesics emanating from  $p$  by  $s_c$ , uniqueness of GPC is achieved. More precisely we limit ourselves to the reduced region

$$R_p := \left\{ (s, \varphi) : \varphi \in S^1, s \leq s_c(\varphi) \right\}.$$

Thereby the set

$$G_p := \left\{ (s_c(\varphi), \varphi) : \varphi \in S^1 \right\}$$

becomes the boundary of our GPC visualization, which by construction is mapped via  $\gamma$  onto the cut locus  $C_p$ . Introducing an equivalence relation  $\sim$  on  $G_p$  such that  $(s_1, \varphi_1) \sim (s_2, \varphi_2)$  iff  $\gamma(s_1, \varphi_1) = \gamma(s_2, \varphi_2)$  one can show that  $R_p$  becomes homeomorphic to  $M$  via the identification  $\sim$ . Thereby one can consider  $G_p$  to be a gluing seam in order to obtain  $M$  from the contractible topological cell  $R_p$ . This especially yields a natural parametrization of  $M$  via  $\gamma : R_p \rightarrow M$ . For the details and a proof working in general settings we refer to [31–33]. Here we illustrate the aforementioned gluing construction schematically in Fig. 11 for the sphere, in Fig. 10 for the cylinder and in Fig. 12 for an ellipsoidal resp. parabolical shape.

**Fig. 10** The cut locus of the cylinder  $M$  considered as a gluing seam

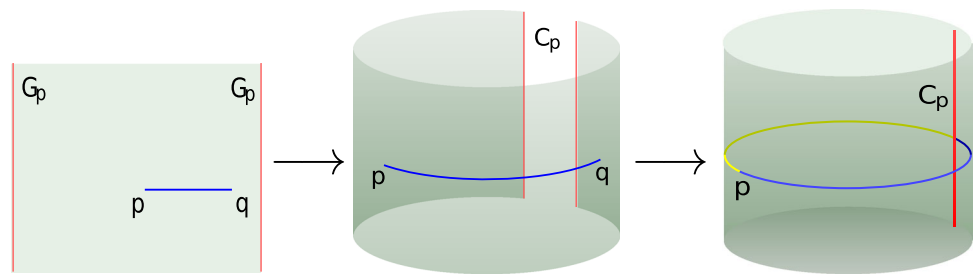


**Fig. 11** The cut locus of a sphere considered as a gluing seam

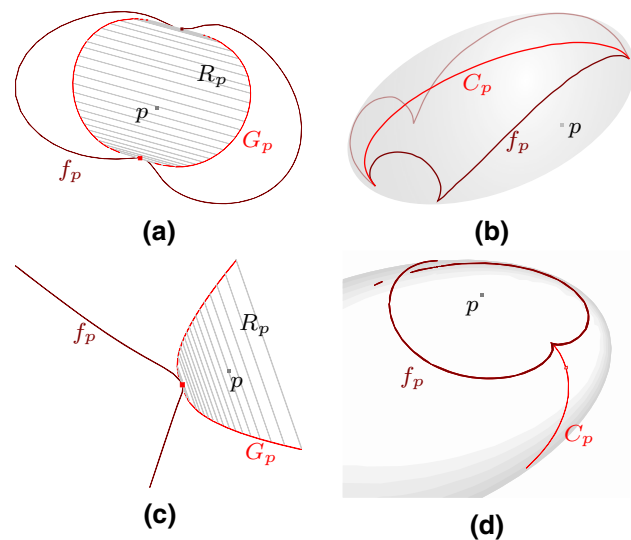
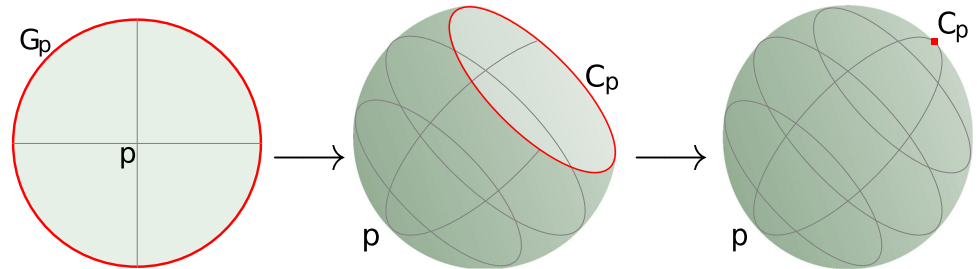


**Fig. 12** Illustration of the cut locus (light red) as a natural gluing seam on an ellipsoidal resp. parabolic shape taken from [9]

Note that in order to compute cut loci several methods have been proposed, see, e.g. [2, 16–18, 20–22, 25, 36]. Returning to the example in Fig. 13, we have used results kindly provided to us by the first author of [25] to obtain the cut locus and use it to eliminate the redundancy, yielding the reduced region depicted in Fig. 13c.

The discussion on the combination of GPC with their associated cut loci indicates its potential for parametrizing manifolds implicitly defined by nonlinear equations and especially yields parametric access to relevant geometric entities such as the jump and hit sets considered. However, due to their generality, we expect the proposed methods to be applicable in a broad context dealing with dynamical systems on implicitly defined manifolds.

### 6 Examples

Our approach has been implemented into a generic and flexible software platform written in C++ allowing us to apply the proposed methods. For some of our numerical computations we relied upon the Gnu Scientific Library (GSL) while our visualization of the high-dimensional results has been implemented in OpenGL. To promote the reproducibility of the results, also a scripting language has been incorporated into the framework.

In order to outline the scope of our methods we will now briefly discuss several examples taken from different scientific fields, illuminating that the approach adopted in this work is flexible enough to deliver numerical results in a variety of practical settings. Although the given examples are only qualitatively discussed, they are taken from applied contexts, incorporating the corresponding physical parameters, such as material constants, etc. In particular, the images are designed to give a qualitative impression of the underlying accurately calculated quantitative results.

The depicted state manifolds are only included for a better understanding as commonly sketched in classical related literature, such as [30].

#### 6.1 Artificial DAE system

As a first example for illustrating our approach, we consider the artificial DAE system given by

$$\begin{aligned} 0 &= z^3 - yz^2 + x \\ \dot{x} &= y \\ \dot{y} &= -x \end{aligned}$$

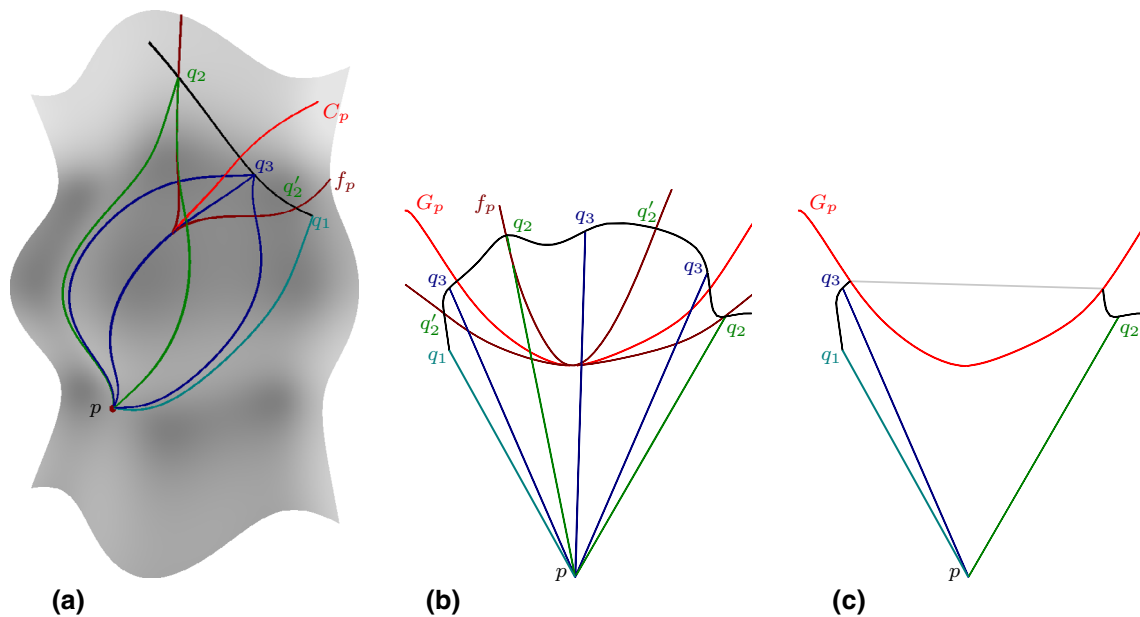


**Fig. 13** Example of local non-uniqueness of GPC. Pictures taken with permission from [25]. **a** Picture on  $M$ . **b** Redundant GPC visualization. **c** Redundant GPC visualization

Here the first equation describes the two-dimensional slow manifold embedded in a three-dimensional space while the other two equations describe a slow vector field curling around the  $z$  axis. It is assumed that the fast vector field points along the  $z$  axis, thus inducing jumps in  $z$  direction. Performing the computations described in the previous sections we obtain the results depicted in Fig. 3.

By introducing an additional parameter  $w$  we lift the above system to create a second example in which the co-dimension of the slow manifold  $M$  is increased from one to two. Thus  $M$  is still two-dimensional while being embedded in a four-dimensional space. The considered equations are

$$0 = z^3 - yz^2 - \frac{1}{2}w + \frac{\sqrt{3}}{2}x$$

$$0 = \frac{\sqrt{3}}{2}w + \frac{1}{2}x$$

$$\dot{x} = -y$$

$$\dot{y} = x$$

We assume the jump space to be spanned by the  $w$  and  $z$  axes. Figure 14 illustrates the individual steps of our approach in this case, showing a three-dimensional projection of the four-dimensional situation.

### 6.2 Heartbeat

In [38] Zeeman discusses a DAE system which is used to model the beating of the heart. In this model, the heartbeat depends on a tension parameter  $a$  and a chemical control parameter  $b$ . These two parameters span the so-called control

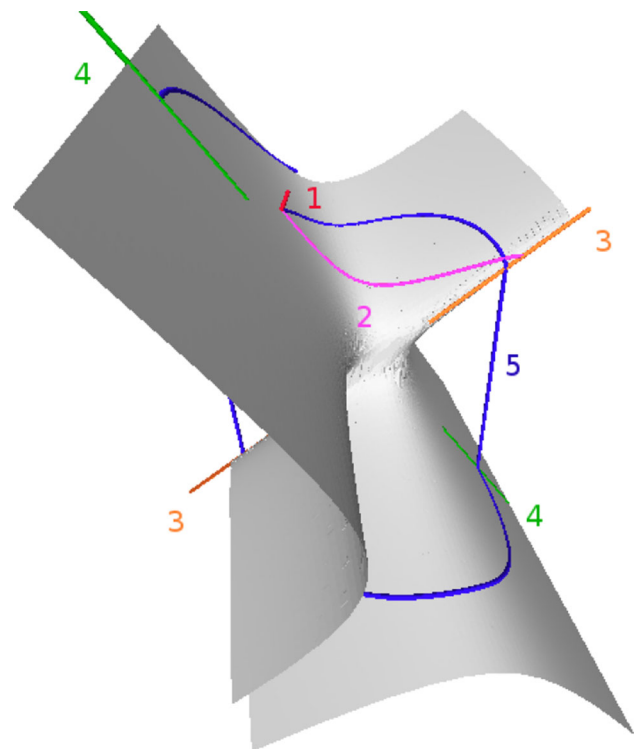


**Fig. 14** Artificial 4D example. 1 Homotopy path leading to an initial point  $p$  on  $M$ . 2 Geodesic used to find an initial point on the jump set. 3 Jump set. 4 Corresponding hit set. 5 Trajectory of the slow vector field on  $M$  starting from  $p$  incorporating two jumps

plane and determine the length of the muscle fiber, denoted by  $x$ . The dynamical behavior is expressed in terms of a slow-fast vector field in the  $(a, b, x)$  space as

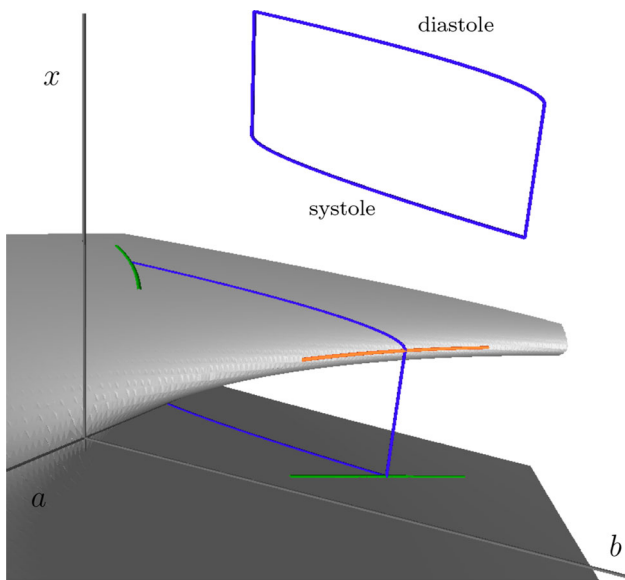


**Fig. 15** Results of computations performed using our approach based on equations presented in [38] for describing the beating of the heart. The closed trajectory in blue represents one cycle of the heartbeat. The jump and hit set are shown in orange and green respectively

$$\begin{aligned} \epsilon \dot{x} &= -(x^3 + ax + b) \\ \dot{b} &= x - x_a \\ \dot{a} &= 0 \end{aligned}$$

Here  $x_a$  denotes the diastole length of the fiber. Letting  $\epsilon \rightarrow 0$  yields the equation of the slow manifold as

$$x^3 + ax + b = 0.$$

Note that the output value  $x$  is needed to calculate  $\dot{b}$ , so the vector field can not be expressed solely in terms of the control parameters.

Figure 15 shows the resulting manifold  $M$ , the jump and hit set as well as a trajectory starting from an initial point on  $M$ , computed using our approach. Note that a part of the jump set is hidden behind the fold of  $M$  and thus not visible from the chosen point of view. The trajectory consists of four parts. Two of those lie on  $M$  and are determined by the slow vector field while the other two are jumps approximating the fast vector field. The trajectory is closed, thereby representing one full cycle, i.e. systole and diastole, of the heartbeat.

### 6.3 Local nerve impulse

Another example discussed in [38] is concerned with modeling nerve impulses in axons. It is based on experiments performed by Hodgkin and Huxley in the 1950s, see [11, 12]. An extended discussion of this model can also be found in [23]. Without going into details, the system can be formulated mathematically in terms of the following slow-fast vector field

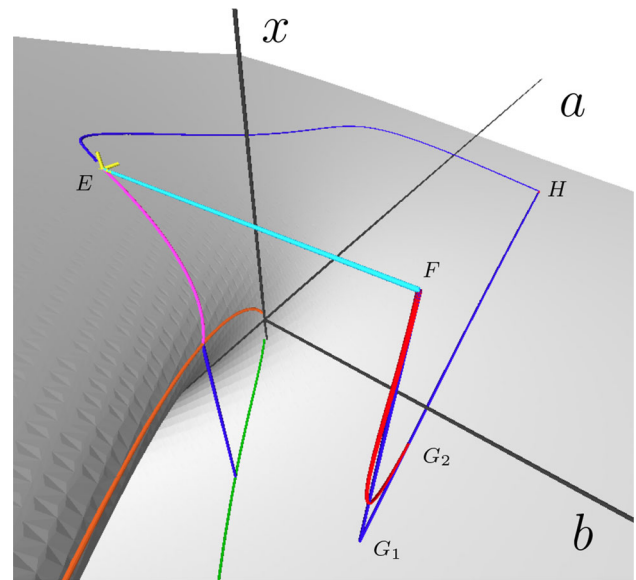


**Fig. 16** Results of modeling the nerve impulse along an axon, obtained using our approach. The underlying model is based on [11, 12, 23, 38]

$$\begin{aligned} \dot{x} &= -\frac{1}{\epsilon}(x^3 + ax + b) \\ \dot{a} &= (x + 0.06(a + 0.5))(x - 1.5a - 1.67) \\ &\quad (0.054(b - 0.8)^2 + 0.75) \\ \dot{b} &= -g_K(b + 1.4) - g_{Na}(b - 4.95) - 0.15(b - 0.15), \end{aligned}$$

where the values of  $g_K, g_{Na}$  depend on  $a$  and  $x$  and are given by

$$g_K = 2.38 \max(a + 0.5, 0), \quad g_{Na} = 16 \min(x + 0.5, 0)^2.$$

As before, the slow manifold  $M$  is obtained by letting  $\epsilon \rightarrow 0$  yielding  $x^3 + ax + b = 0$ .

Consider Fig. 16 showing  $M$  with the jump set (orange) and hit set (green) computed using our approach. From any point on  $M$  the slow dynamic given above leads to the equilibrium point  $E$  which represents a kind of resting state of the nerve. The application of external influences to the physical system can be modeled by changing the slow vector field. For example, referring to the “voltage clamp experiment” described in [38] applying an external voltage to the nerve displaces the system from  $E$  to the point  $F$ , thus leaving the manifold. While retaining the constraint  $b = const.$ , the dynamic of the system leads to the point  $H$ . Here  $\epsilon = 0.2$  was used. Note that in this example, the vector field is effectively modified by setting  $\dot{b} = 0$ . The point  $H$  is an equilibrium of the modified vector field. By switching off the external voltage, the aforementioned constraint is eliminated, thereby allowing the system to return to the equilibrium point  $E$  of the original vector field.

As the trajectory from  $F$  to  $H$  is dominated by the fast component of the vector field in  $x$  direction, it is natural to

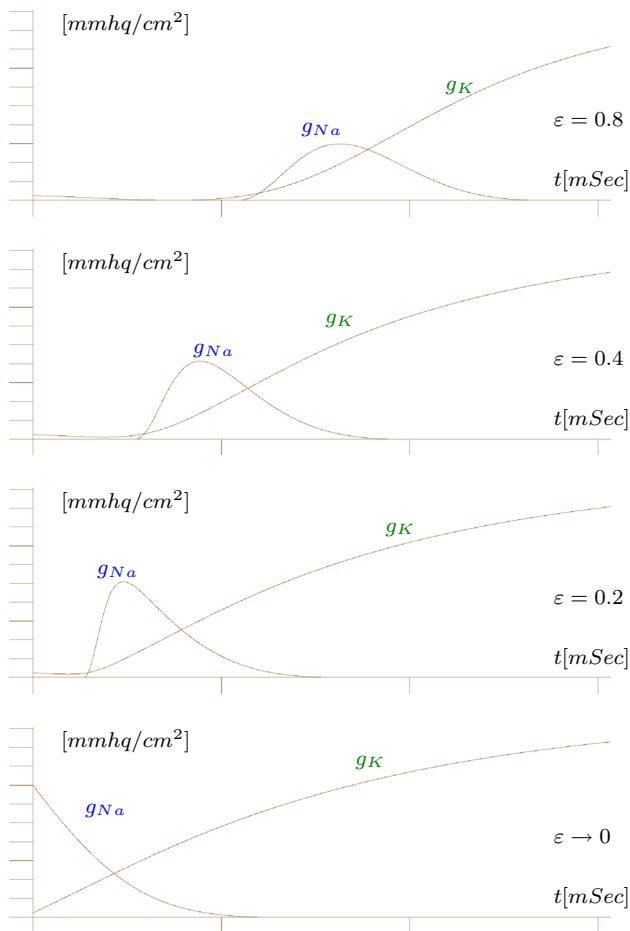


**Fig. 17** Computed action potentials for the local nerve impulse example for different values of  $\epsilon$ . The last picture shows a jump from  $F$  to  $G_1$ , see Fig. 16

consider a jump from  $F$  to  $G_1$ , followed by the trajectory of the modified slow vector field leading to  $H$  along  $M$ . Both paths are depicted in the figure in red resp. blue.

A plot of the resulting quantities  $g_{Na}$  and  $g_K$  along the computed trajectories is known as the so-called action potentials and depicted in Fig. 17. These results are consistent with the discussion of Woodcock, see in particular Figs. 19 and 20 in [23] where a clamp voltage of 38mV has been used.

### 6.4 Electrical circuits

Parts of the presented framework have been applied in the context of studying examples taken from electrical engineering, see, e.g. [14,27,29]. A main objective in this context is to determine stable operating points of electrical circuits. The conventional design cycle employs circuit simulators for this purpose, which unfortunately are known to fail for certain idealized circuits. Common methods to overcome this difficulty employ heuristics to facilitate the convergence of the simulations which depend on introducing parasitic

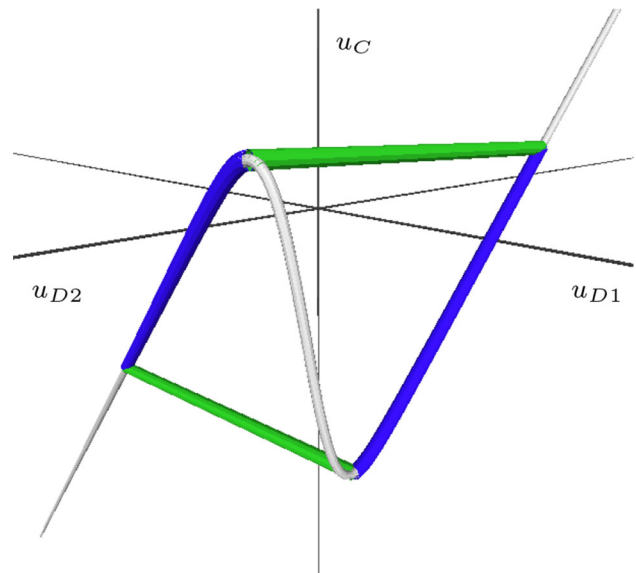


**Fig. 18** Closed limit cycle of a multi-vibrator with one capacitance. The state manifold, the trajectory of the slow vector field and the jumps are indicated in gray, blue and green, respectively

inductances and capacitances into the circuit layout. While from a mathematical perspective the latter approach corresponds to the so-called Tikhonov regularization, it is unsatisfactory in practice since it depends essentially on the experience of the designer and is prone to error. For more background related to these issues we refer to [26,28].

Our approach allows to determine operating points of electrical circuits without using parasitic elements and the corresponding regularization techniques.

Figure 18 shows an example modeling an emitter-coupled multi-vibrator discussed in [27]. The governing equations are given by a DAE system of the form

$$f(u_{D1}, u_{D2}, u_C) = 0, \quad g(u_{D1}, u_{D2}, u_C, \dot{u}_C) = 0.$$

The specific expressions for  $f$  and  $g$  can be found in [27]. In this example the slow manifold  $M$  is the one-dimensional curve shown in gray, while jump and hit sets are zero-dimensional, consisting of isolated points on  $M$ . The jump space is spanned by the  $u_{D1}$  and  $u_{D2}$  directions.

As a second example we consider a MOS flip flop model, see [29], which is characterized by a one-dimensional state manifold embedded in a four-dimensional space spanned by the parameters denoted as  $u_{GS1}, u_{GS2}, u_{in}, u_{out1}$ . The jump space here is three dimensional and spanned by the  $u_{GS1}, u_{GS2}$  and  $u_{out1}$  directions. The corresponding result is shown in Fig. 19.

### 6.5 Euler arch

As an example for a mechanical system we consider the Euler Arch adapted from [38]. It consists of two rigid arms being

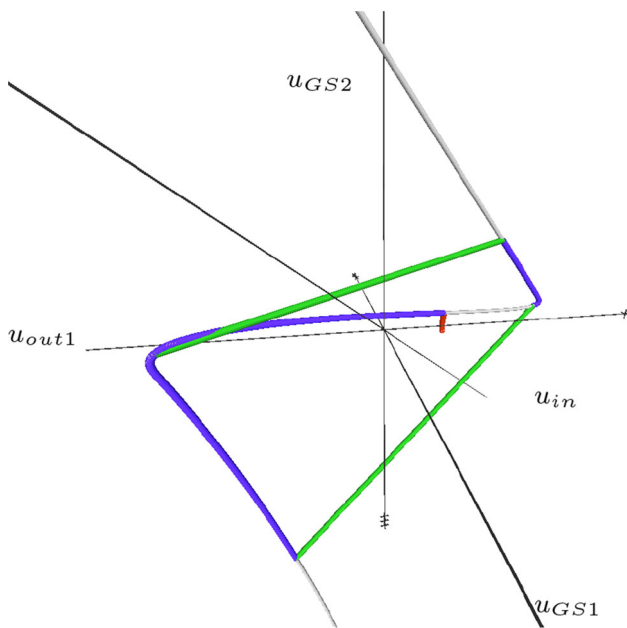


**Fig. 19** Visualization of the MOS flip flop model described in [29] with colors as in Fig. 18. Additionally, the homotopy path leading to an initial point on  $M$  is shown in red

connected by a spring of stiffness  $\mu$  that tends to keep them aligned. There is one force  $F_x$  compressing the two arms and another force  $F_y$  acting from the top. The position of the arms can be described using an angle parameter  $\alpha$  as shown in Fig. 20a. Increasing the force  $F_x$  makes the construction buckle upwards, while increasing  $F_y$  leads to the so-called catastrophe in which the arch suddenly jumps into a state buckling downwards. As discussed in [38], the set of valid states  $(F_x, F_y, \alpha)$  is a two-dimensional manifold described by the equation

$$4\mu\alpha + F_y \cos(\alpha) - 2F_x \sin(\alpha) = 0$$

We extend this example by modeling a feedback system in terms of a vector field, thereby equipping the manifold with a dynamic. If  $F_x$  is low, the feedback system will increase it. As  $F_x$  reaches a designated value, the variation of  $F_x$  slows down smoothly while  $F_y$  starts to increase. As  $F_y$  increases, the system finally reaches a situation as described above, where a sudden jump has to occur. We model this behavior using the following slow vector field:

$$\dot{F}_x = \frac{1}{e^{2(F_x-3.25)} + 1} \quad \dot{F}_y = 10 - \frac{20}{e^{2(F_x-3.25)} + 1}.$$

Figure 21 visualizes the results of the corresponding computations.

### 6.6 Extended Euler arch

In this final example we extend the model of the Euler arch described in the previous section by introducing a new degree

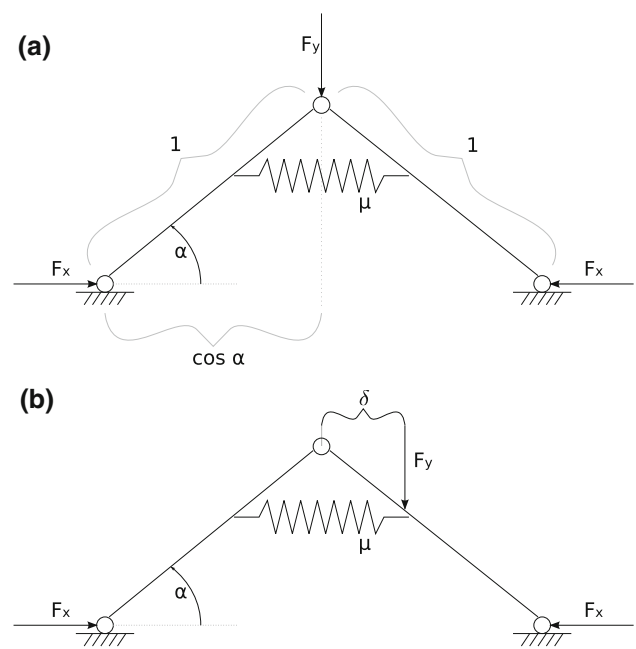


**Fig. 20** a Euler arch. b Extended Euler arch

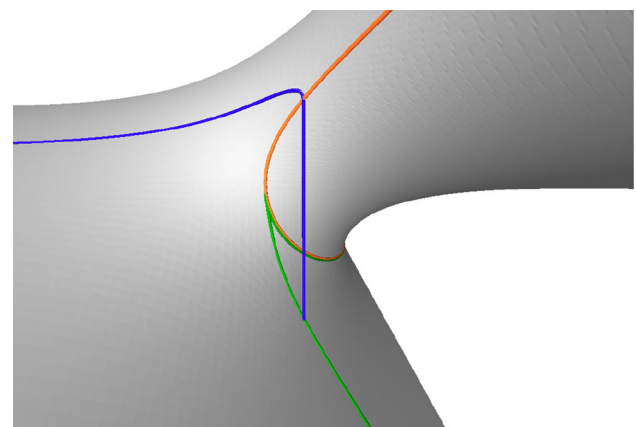


**Fig. 21** Results of modeling the Euler arch based on the discussion in [38]. The blue path represents the trajectory of the given slow vector field incorporating a jump

of freedom  $\delta$  that denotes the horizontal distance from the center to the position where  $F_y$  is applied. Thus  $F_y$  may act at a point differing from the center as shown in Fig. 20b.

By a derivation similar to [38] we arrive at the following equation implicitly characterizing the system's set of admissible states as a three-dimensional manifold embedded in four-dimensional Euclidean space whose axes are identified with the parameters  $\alpha, F_x, F_y$  and  $\delta$ :

$$(4\mu\alpha - 2F_x \sin(\alpha)) \cos^2(\alpha) + F_y(\cos^3(\alpha) - \delta) = 0.$$

By applying our computational methods, we could successfully determine initial points on the manifold and on the jump set  $\alpha$ , resp. on the hit set  $\beta$ . Note that the latter sets are two



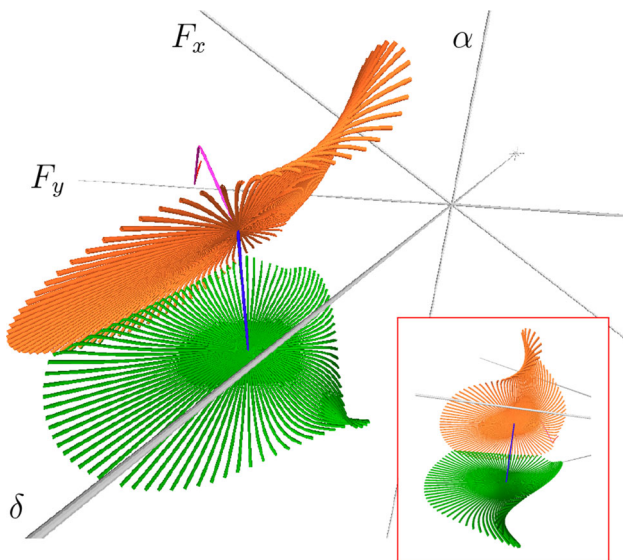


**Fig. 22** Two-dimensional jump set (*orange*) and the corresponding hit set (*green*) of the state manifold for the extended Euler arch example

dimensional in this example. Thus, as discussed in Sect. 3.5, we have relied upon geodesic polar coordinates to parametrize  $\alpha$  while tracing the corresponding projections on  $\beta$  in parallel. The result of this approach is illustrated in Fig. 22, showing a projection of the four-dimensional space.

## 7 Conclusion and outlook

In this work we have discussed how a toolkit of geometrically inspired methods can be used to analyze a variety of dynamical systems governed by slow–fast vector fields and corresponding systems of differential algebraic equations.

Our approach consists in explicitly computing jump and hit sets on the slow manifold  $M$ , allowing us to capture the dynamics of the corresponding model by tracing the slow component of the vector field along  $M$  while incorporating jumps in direction of the fast component.

Note that while the state manifolds depicted in our examples require a sampling for visualization, our presented methods do not depend on them. They rely only upon a comparatively localized evaluation of the equations describing the given DAE system. In fact the particular representation of the underlying functions describing our DAE system does not matter. Therefore, the presented approach scales efficiently to higher dimensions as realized in our framework.

As the considered equations are in general nonlinear, our approach incorporates extended homotopy methods to determine initial points and exploits numerical continuation techniques as well as geodesic polar coordinates to obtain explicit parametrizations. Our methods are numerically stable and improve upon classical approaches which trace the

slow–fast vector field directly and therefore suffer from the large gap between the involved scales.

In the future we plan to further optimize our approach involving geodesic polar coordinates by taking into account the non-injectivities induced by them. As indicated within the discussion in Sect. 5 concepts such as the cut-locus and focal sets have to be considered. It remains a promising topic for future research to further exploit the potential of these local and global concepts for a dimensionality-reduction purposes and an analysis of the global topological and geometrical features of  $M$ .

**Acknowledgments** The research in this article was partially supported by the German Research Foundation (DFG), Project “Differentialgeometrische Methoden zur Analyse nichtlinearer elektronischer Schaltungen und deren Visualisierung”.

## References

- Allgower, E.L., Georg, K.: Introduction to numerical continuation methods. Classics in applied mathematics. SIAM (2003). doi:10.1137/1.9780898719154.
- Dey, T.K., Li, K.: Cut locus and topology from surface point data. Proceedings of the Twenty-fifth Annual Symposium on Computational Geometry. SCG '09, pp. 125–134. ACM, New York (2009)
- do Carmo, M.P.: Riemannian Geometry. Birkhauser, Boston (1992).
- Golub, G., Kahan, W.: Calculating the singular values and pseudo-inverse of a matrix. J. SIAM Numer. Anal. Ser. B **2**, 205–224 (1965)
- Guckenheimer, J., Haiduc, R.: Canards at folded nodes. Mosc. Math. J. **5**(1), 91–103 (2005)
- Guckenheimer, J., Hoffman, K., Weckesser, W.: Numerical computation of canards. Int. J. Bifurc. Chaos **10**(12), 2669–2687 (2000)
- Guckenheimer, J., Hoffman, K., Weckesser, W.: Global analysis of periodic orbits in the forced van der Pol equation. In: Broer H.W., Krauskopf B., Vegter G. (eds.) Global Analysis of Dynamical Systems-Festschrift Dedicated to Floris Takens for his 60th Birthday, pp. 261–276. IOP Press (2003)
- Guillemin, V., Pollack, A.: Differential Topology, vol. 370. American Mathematical Society. (Englewood Cliffs, N.J.: Prentice-Hall, 1974) (2010)
- Gutschke, M.: Untersuchungen zur Berechnung kürzester Verbindungswege auf gekrümmten Flächen. Diploma thesis, Welfenlab, Leibniz Universität Hannover (2004).
- Gutschke, M., Vais, A., Wolter, F.-E.: A geometrical framework to capture the dynamical evolution of slow-fast vector fields. In: Proceedings NASAGEM Workshop-Computer Graphics International (2013). <http://welfenlab.de/fileadmin/gutschke2013.pdf>. Accessed 11 June 2013
- Hodgkin, A.L., Huxley, A.F.: A quantitative description of membrane current and its application to conduction and excitation in nerve. J. Physiol. **117**, 500–544 (1952)
- Hodgkin, A.L., Huxley, A.F.: Currents carried by sodium and potassium ions through the membrane of the giant axon of Loligo. J. Physiol. **116**, 449–472 (1952)
- Katok, A., Hasselblatt, B.: Introduction to the Modern Theory of Dynamical Systems, vol. 54. Cambridge University Press, Cambridge (1997)

14. Mathis, W., Blanke, P., Gutschke, M., Wolter, F.-E.: Nonlinear electric circuit analysis from a differential geometric point of view. *ITG-Fachbericht-ISTET* **2009**, 30167 (2009)
15. Memoli, F., Sapiro, G., Osher, S.: Solving variational problems and partial differential equations mapping into general target manifolds. *J. Comput. Phys.* **195**, 263–292 (2004)
16. Nass, H.: Medial axis on Riemannian manifolds. Ph.D. thesis, Leibniz Universitaet Hannover (2007).
17. Nass, H., Wolter, F.-E., Dogan, C., Thielhelm, H.: Computation of geodesic voronoi diagrams in 3-space using medial equations. In: *Proceedings of NASAGEM*, 26 Oct 2007 (2007).
18. Nass, H., Wolter, F.-E., Thielhelm, H., Dogan, C.: Medial axis inverse transform in 3-dimensional riemannian complete manifolds. In: *Proceedings of NASAGEM*, Hannover, 26 Oct 2007 (2007).
19. Poincaré, H.: Sur les Lignes Géodésiques des Surfaces Convexes. *Trans. Am. Math. Soc.* **6**, 237–274 (1905)
20. Rausch, T.: Untersuchungen und Berechnungen zur Medialen Achse bei berandeten Flaechenstuecken. Ph.D. thesis, Universitaet Hannover (1999).
21. Rausch, T., Wolter, F.-E., Sniehotta, O.: Computation of medial curves on surfaces. *Math. Surf.* **7**, 43–68 (1997)
22. Sinclair, R., Tanaka, M.: Loki: software for computing cut loci. *Exp. Math.* **11**(1), 1–25 (2002)
23. Steward, I., Woodcock, A.E.R.: On Zeeman's equations for the nerve impulse. *Bull. Math. Biol.* **43**, 279–325 (1981)
24. Tchizawa, K.: An analysis of nonlinear systems with respect to jump. *Yokohama Math. J.* **32**, 203–214 (1984)
25. Thielhelm, H., Vais, A., Brandes, D., Wolter, F.-E.: Connecting geodesics on smooth surfaces. *Vis. Comput.* **28**(6–8), 529–539 (2012)
26. Thiessen, T.: Mathis: geometric dynamics of nonlinear circuits and jump effects. *Int. J. Comput. Math. Electr. Electron. Eng.* **30**(4), 1307–1318 (2011)
27. Thiessen, T., Gutschke, M., Blanke, P., Mathis, W., Wolter, F.-E.: Numerical analysis of relaxation oscillators based on a differential geometric approach. In: *International Conference on Signals and Electronic Systems*, pp. 209–212 (2010).
28. Thiessen, T., Gutschke, M., Blanke, P., Mathis, W., Wolter, F.-E.: A numerical approach for nonlinear dynamical circuits with jumps. In: *European Conference on Circuit Theory and Design* (2011).
29. Thiessen, T., Gutschke, M., Blanke, P., Mathis, W., Wolter, F.-E.: Differential geometric methods for jump effects in nonlinear circuits. In: *20th Edition of the Nonlinear Dynamics of Electronic Systems* (2012).
30. Thom, R.: *Structural Stability and Morphogenesis*. W.A. Benjamin, inc., Advanced Book Program, Reading (1975)
31. Wolter, F.-E.: Distance function and cut loci on a complete Riemannian manifold. *Arch. Math.* **1**(32), 92–96 (1979)
32. Wolter, F.-E.: Cut loci in bordered and unbordered Riemannian manifolds. Ph.D. thesis, TU Berlin (1985).
33. Wolter, F.-E.: Cut locus and medial axis in global shape interrogation and representation. MIT Design Laboratory Memorandum 92–2 and MIT National Sea Grant Library Report. MIT, Dec 1993 (1992) (revised version).
34. Wolter, F.-E., Tuohy, S.T.: Approximation of high-degree and procedural curves. *Eng. Comput.* **8**(2), 61–80 (1992)
35. Wolter, F.-E., Tuohy, S.T.: Curvature computations for degenerate surface patches. *Comput. Aided Geom. Des.* **9**(4), 241–270 (1992)
36. Wolter, F.-E., Blanke, P., Thielhelm, H., Vais, A.: Computational differential geometry contributions of the welfenlab to grk 615. In: *Modelling, Simulation and Software Concepts for Scientific-Technological Problems*, vol. 57, pp. 211–235. Springer (2011).
37. Zangwill, W.I., Garcia, C.B.: *Pathways to solutions, fixed points, and equilibria*. Prentice-Hall, Englewood Cliffs (1981)
38. Zeeman, E.C.: *Catastrophe Theory: Selected Papers, 1972–1977*. Addison-Wesley, Reading (2000).



**Martin Gutschke** gained a diploma in Electrical Engineering from the Leibniz University of Hannover (LUH) in 2004. He is currently a Ph.D. student at LUH Division of Computer Graphics. His main interests is computational differential geometry.



**Alexander Vais** gained B.Sc. and M.Sc. degrees in Computer Science from the Leibniz University of Hannover (LUH) in 2007 and 2009, respectively. He is currently a Ph.D. student at LUH Division of Computer Graphics. His main interests are computational differential geometry and geometry processing algorithms.



**Franz-Erich Wolter** has been Chaired Full Professor of Computer Science at Leibniz University Hannover since 1994 where he directs the Division of Computer Graphics called Welfenlab. He held faculty positions at University of Hamburg (1994), MIT (1989–1994) and Purdue University USA (1987–1989). He was software and development engineer with AEG (Germany) (1986–1987). Dr. Wolter obtained his Ph.D. (1985) mathematics, TU Berlin, Germany, in the area of Riemannian manifolds, Diploma (1980), FU Berlin, mathematics and theoretical physics. At MIT he co-developed the geometric modeling system Praxiteles for the US Navy and published papers that broke new ground applying concepts from differential geometry and topology on problems in geometric modeling. Dr. Wolter is research affiliate of MIT.